RESEARCH ARTICLE

JOURNAL OF **Applied Polymer** SCIENCE **WILEY**

Large strain mechanical behaviors of optically clear adhesives for flexible electronic devices under different temperature, humidity, and strain rates

Jinrui Cao[1] | Abuzar Es'haghioskui[1] | Sorour Sadeghzade[1] | Yuanlong Li[1] | Zhaoyan Huang[1] | Xin Li[1] | Peng Dong[1] | Jiayi Hu[1] | Runsheng Hou[1,2] | Hongyan Yuan[1]

[1]Shenzhen Key Laboratory of Soft Mechanics & Smart Manufacturing, Department of Mechanics and Aerospace Engineering, Southern University of Science and Technology, Shenzhen, China

[2]Department of Mechanical Engineering, Virginia Tech, Blacksburg, Virginia, USA

Correspondence
Hongyan Yuan, Shenzhen Key Laboratory of Soft Mechanics & Smart Manufacturing, Department of Mechanics and Aerospace Engineering, Southern University of Science and Technology, Shenzhen 518055, China.
Email: yuanhy3@sustech.edu.cn

Abstract

Optically clear adhesives (OCAs), a type of polymer pressure-sensitive adhesive, are valued for their transparency, strong bonding, thermal stability, and reliability in flexible electronics. Accurately determining the mechanical properties of OCAs is importance for effectively assessing the structural integrity of foldable screens in finite element simulations. However, previous studies have primarily focused on small strain and conventional environmental conditions. To address this gap, the present study investigates the mechanical behaviors of OCAs under extreme conditions, including large strain (up to 1000%), high/low temperatures (−40, −20, 0, 25, 65, and 80°C), and high humidity (95% relative humidity). Specifically, the tensile, simple shear, and creep properties of OCAs have been assessed in an attempt to explore their visco-hyperelastic behavior. The experimental findings indicate that OCA exhibits noticeable temperature sensitivity and viscoelasticity, along with volume-incompressible properties. Notably, when the temperature is varied from −40 to 25°C and from 25 to 80°C, the modulus of OCA experiences an average reduction of 84% and 41% respectively. Moreover, it has been observed that humidity has a negligible effect on the material's modulus. The Yeoh model and Prony series are employed for fitting purposes. The proposed fitting parameters are subsequently validated through numerical simulations of three-point bending case studies. Remarkably, the simulation results closely matched with the experimental data, with errors remaining below 10%.

KEYWORDS
adhesives, mechanical properties, viscosity and viscoelasticity

1 | INTRODUCTION

Optically Clear Adhesives (OCAs),[1–3] acrylic-based polymers,[4,5] have widespread applications in the realm of flexible electronics, particularly in the construction of foldable organic light-emitting diode (OLED)[6] and active-matrix organic light-emitting diode (AMOLED) screens.[7,8] Possessing transparency and robust adhesive strength, OCAs serve as pressure-sensitive adhesives (PSAs). In the context of foldable screens, their primary

role is to facilitate the bonding of diverse, rigid functional layers.[9] Simultaneously, owing to their softness and favorable fluidity, OCAs adeptly address misalignments among functional layers during the folding process.[10,11] This capability engenders a multi-neutral layer effect, mitigates strain, and safeguards the constituent components of the screen. It can be asserted that OCA materials play a crucial role in realizing flexible and bendable screens, and investigating their mechanical behaviors holds substantial significance.[12]

OCA, being a polymer, inherently displays temperature sensitivity, resulting in notable changes in its mechanical properties in response to variations in temperature. In the context of foldable screens, the material experiences a broad temperature range, with the minimum operating temperature in polar regions reaching as low as $-40°C$. Conversely, during elevated temperatures in summer, heat dissipation from other system components[13] may exceed $80°C$. Within the temperature range of -40 to $80°C$, OCA displays notable variations in mechanical behavior. Consequently, a thorough examination of the impact of OCA on materials at both low and high temperatures becomes imperative. Zhang et al.[14] conducted an investigation into the storage modulus and glass transition temperature of OCA across a temperature range spanning -40 to $120°C$. They subsequently constructed a master curve using the Williams–Landel–Ferry (WLF) equation to capture the material's response across the entirety of the temperature domain. However, the WLF equation is founded on assumptions of linear viscoelasticity and small strain,[15] characteristics not applicable to OCA due to substantial nonlinear changes within extensive temperature ranges. Moreover, the method employing the WLF equation allows for the determination solely of the storage modulus at specific temperatures, precluding the derivation of the stress–strain curve under conditions of large strain loading. Considering that OCA will withstand over 500% strain in finite element simulation,[16,17] the aforementioned testing approach is not directly suitable. Hence, it is imperative to conduct large strain loading at various temperatures and subsequently fit the constitutive parameters under large strain, examining the temperature-induced variations in material modulus.

Humidity variations in the environment may also exert a notable influence on the mechanical properties of polymers.[18] Chen et al. explored the effects of extended exposure to high temperature and humidity on the strength of soy protein adhesives, which share a similar microstructure with OCA. The study revealed a decline in shear strength over exposure time, mainly due to hydrolysis, oxidation, and hydrogen bond dissociation in the adhesive, leading to reduced crosslinking density and intermolecular forces.[19] In high-humidity environments,

the use of flexible equipment is susceptible to moisture influence, leading to the erosion of the polymer network by water vapor and consequently diminishing the performance of OCA. However, there is still a lack of research findings on the mechanical properties of OCA in high-humidity environments, especially the mechanical performance of OCA in conditions characterized by high temperatures and high humidity.

Additionally, the instinctive viscoelasticity[20–22] of OCAs results in varied mechanical responses under different strain rates, with the material exhibiting relaxation and creep over time under loading conditions.[23] In the context of a flexible folded screen, OCA experiences stress and strain, demonstrating stress relaxation and creep phenomena during the folding process. In the simulation and design of foldable screens, the analysis of these phenomena becomes imperative, necessitating the establishment of a viscoelastic constitutive model for implementation in finite element analysis. Li et al.[24] formulated a transversely isotropic and rate-dependent phenomenological constitutive model tailored for OCA, utilizing true stress and true strain as the basis. Wang et al.[25] and Jia et al.[26] also fitted the viscoelastic constitutive model in their research, and based on the generalized Maxwell model, the classic Prony series was fitted. The aforementioned studies were exclusively conducted at room temperature, omitting the consideration of the impact of temperature on viscoelasticity.[27,28] Furthermore, during the folding of the screen, OCA experiences a substantial strain rate, reaching approximately the $\sim1\ s^{-1}$ level. Traditional quasi-static loading methods are inadequate for reproducing the real-world application scenarios of this material, high strain rate loading (like $5\ s^{-1}$) must be carried out.

Developing an innovative approach to characterize the mechanical behavior of OCA is critical,[29] encompassing key factors for a comprehensive evaluation of its properties. It needs to consider the following factors: (1) The stress–strain relationship of materials under large strain, necessitating the adoption of a hyperelastic constitutive model,[30] rather than merely simplifying the mechanical behaviors in terms of modulus.[31,32] (2) Mechanical behaviors corresponding to distinct temperatures should be characterized separately, involving the fitting of corresponding constitutive parameters for simulation purposes. The application of the time–temperature equivalence theory, as done in the WLF equation, is deemed unsuitable for simplifying the global temperature into several parameters. (3) Extraction methods for fitting experimental data and validation techniques should be considered to accurately determine the constitutive parameters. (4) A systematic mechanical characterization of OCA should be conducted under
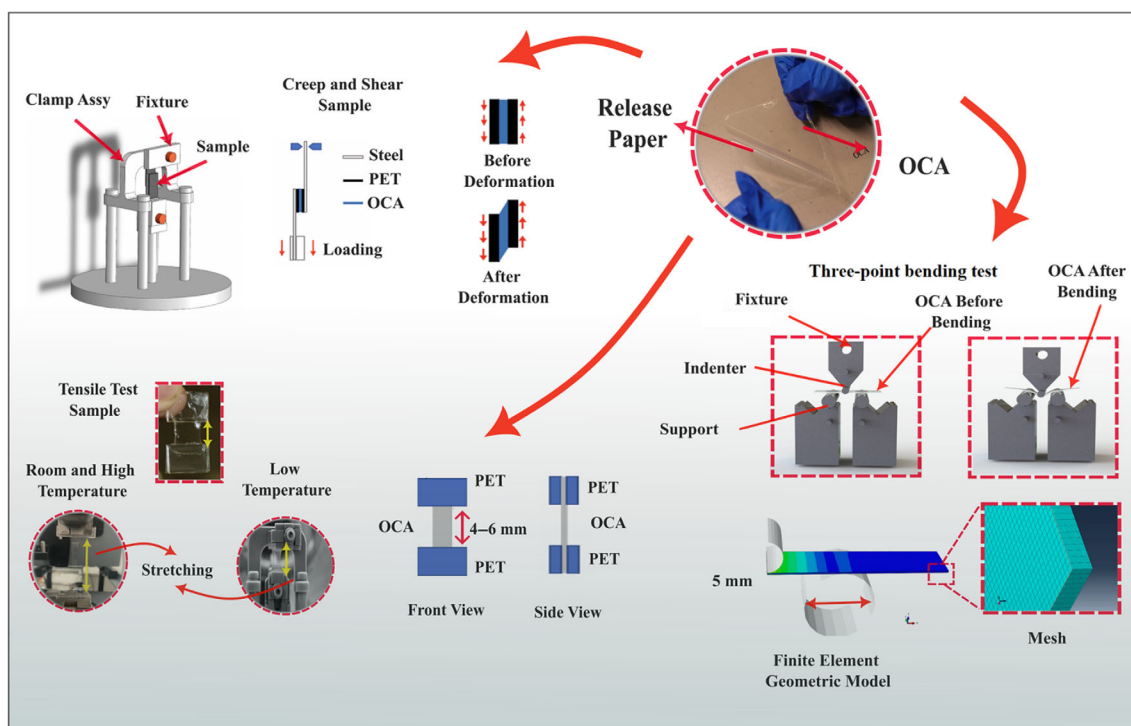
FIGURE 1 Schematic representation of typical commercial optically clear adhesive (OCA, 3 M) and various static and dynamic mechanical analysis loading for different mechanical tests (tensile, shear, creep, and bending) in various conditions. [Color figure can be viewed at wileyonlinelibrary.com]

extreme conditions, encompassing various parameters such as temperature, strain rates, and humidity levels.

This study provides a comprehensive mechanical analysis of commercially available OCA for flexible electronics using both experimental and numerical methods. It investigates the material's behavior under varying temperature ranges, humidity levels, and strain rates. The main tests encompassed shear, tensile, and creep loading modes. Time-stress–strain curves were extracted to characterize the material's response under these specified loading conditions. Additionally, the Poisson's ratio of the material was measured to provide comprehensive insights into its mechanical properties. In accordance with this, the hyperelastic and viscoelastic constitutive parameters of the material were calibrated at various temperatures. Subsequently, these constitutive parameters were integrated into the numerical model of three-point bending (3PB). To validate the accuracy of the constitutive calibration, corresponding three-point bending tests were conducted, and the experimental results were compared with simulation outcomes. This study offers a comprehensive examination of the mechanical response of OCA material within practical usage environments. The findings are presented in the form of constitutive parameters, providing valuable information for direct application finite element analysis.

2 | METHODS

2.1 | Mechanical properties

In Figure 1, a widely used commercially OCA (CEF35 from 3M Company, America) is configured into tensile and shear samples and subjected to loading. OCA tests present unique challenges compared with traditional PSA or soft materials testing. These challenges include the low elastic modulus, thin thickness (approximately 25–100 μm), and low bending stiffness of the OCA material, making it prone to deformation. Additionally, the strain state of the viscoelastic material is influenced by its stress history, necessitating the minimization of prestress during loading and preparation. Therefore, conducting OCA tests requires careful consideration and control of these factors to ensure accurate results. Drawing from prior testing experience, numerous testing technologies have been embraced to enhance testing accuracy.[33–35]

The principal variables in the test encompass strain rate, temperature, environment, and others. We systematically conducted tests for the majority of possible combinations of these upstream variables. To mitigate potential confusion, we have precisely defined the conducted tests in Table 1. To evaluate temperature sensitivity, tests were conducted at low (−40, 0, and −20°C), room (25°C), and high (65 and 80°C) temperatures, replicating real-world

TABLE 1 Samples definition under various conditions (strain rate, temperature, and humidity).

Strain rate (s^{-1}) Temperature	5	1	0.1	0.01
−40°C	T-40V5S			
			T-40V0.1T	
−20°C	T-20V5S			
			T-20V0.1T	
0°C	T0V5S			
			T0V0.1T	
25°C	T25V5S	T25V1S	T25V0.1S	T25V0.01S
	T25V5T	T25V1T	T25V0.1T	T25V0.01T
25°C, 95% RH	T25V5HT	T25V1HT	-	-
65°C	T65V5S	T65V1S	T65V0.1S	T65V0.01S
	-	-	-	-
80°C, 95% RH	T80V5S	T80V1S	T80V0.1S	T80V0.01S
	T80V5HT	T80V5HT	-	-

Abbreviation: RH, relative humidity.

usage scenarios. The strain rates were set to 0.01, 0.1, 1, 2, and 5 s^{-1}, encompassing two loading modes: uniaxial tension and simple shear. In partial loading, two additional environments were introduced: room temperature and high humidity (25°C, 95% relative humidity), and high temperature and high humidity (80°C, 95% RH), to investigate the impact of humidity on the material. Creep tests lasting approximately 10 h were conducted at both room temperature and high temperature, with a stress of 50 kPa applied. The time-displacement curve is recorded during the test and subsequently converted into a time-strain curve during post-processing.

The schematic representation of various mechanical loading conditions is illustrated in Figure 1. The samples used for shear and creep tests had dimensions of 10 mm × 10 mm × 0.1 mm (length, width, thickness), while those for tensile were sized at 5 mm × 10 mm × 0.1 mm.[27] Room and high-temperature tensile tests, with and without humidity, were conducted on a universal testing machine (Instron 5966, equipped with a 100 N sensor), as depicted in Figure 1.[36] To enhance the clamping state and alleviate stress concentration at the boundaries, light acrylic plates were used to clamp the upper and lower ends. Low-temperature tensile tests were performed using the Dynamic Mechanical Analyzer (DMA, TA Instruments 850, USA). During shear testing, loading is terminated upon material failure or when the strain attains 1000%. Force-displacement curves are documented throughout the test, and subsequently, during post-processing, they are transformed into nominal stress–strain curves. Preceding the commencement of shear and creep testing, the DMA system adjusts the ambient temperature to the specified value, allowing for a 10-min

period to ensure uniform heating or cooling of the material. Testing initiates thereafter, with the temperature sustained consistently throughout the duration of the test.

Poisson's ratio was calculated through the application of the digital image correlation (DIC) method. The DIC system facilitates the determination of local strain within a defined area by tracking the displacement of speckle patterns, thereby enabling the acquisition of strain values along the loading direction (ε_x) and transverse strain (ε_y). By comparing these strain components, it is possible to obtain the Poisson's ratio:

$$\mu = -\frac{\varepsilon_y}{\varepsilon_x}. \tag{1}$$

When the Poisson's ratio is 0.5, the material is considered completely incompressible. Generally, materials are considered nearly incompressible when the Poisson's ratio μ exceeds 0.45.

2.2 | Constitutive model and calibration

The mechanical constitutive model of OCA comprises two components: hyperelasticity and viscoelasticity, collectively referred to as visco-hyperelasticity. Viscoelasticity refers to the time-dependent behavior of material properties, while hyperelasticity signifies nonlinear elasticity. Figure 2a schematically depicts the molecular network, encompassing crosslinked networks, entanglement networks, and free chains. The microstructures intricately govern the material's macroscopic mechanical response, with the hyperelastic stress originating from the crosslinked network and the viscoelastic stress arising from the free chains.[37,38]

FIGURE 2 (a) The schematic diagram of the polymer chain network with applied deformation and the tube model capturing the constraint effects of a single chain caused by its neighboring chains, (b) Schematic diagram of the generalized Maxwell model. [Color figure can be viewed at wileyonlinelibrary.com]
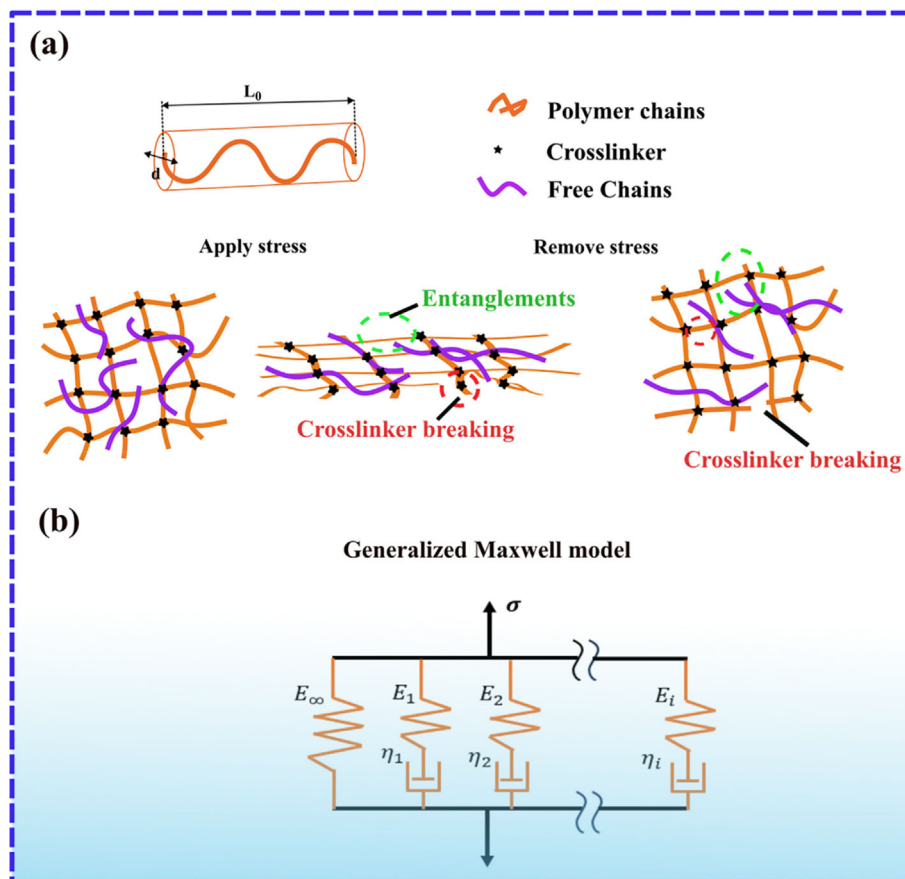
2.2.1 | Hyperelastic part

As illustrated in Figure 2a, long randomly oriented polymer chains are interconnected through cross-linkers, creating a cross-linked polymeric network where free chains are dispersed randomly. During loading or unloading, the cross-linked polymer network undergoes stretching, and the free chains diffuse within the network. The cross-linked polymer network serves as the backbone and typically exhibits the ability to recover its original shape after unloading, leading to a nonlinear hyperelastic mechanical response. In contrast to linear elastic materials, the stress–strain relationship in hyperelastic materials is delineated by the strain energy, expressed in terms of strain invariants, as follows:

$$
W(\bar{I}_1, \bar{I}_2) = \frac{1}{2}\left[\begin{array}{c} a_1(\bar{I}_1 - 3) + \frac{1}{2}a_2(\bar{I}_1{}^2 - 9) + \frac{1}{3}a_3(\bar{I}_1{}^3 - 27) \\ + a_4(\bar{I}_2 - 3) + a_5(\bar{I}_1\bar{I}_2 - 9) \end{array}\right],
\tag{2}
$$

where a_i represents the material parameters, and $\bar{I}_1$ and $\bar{I}_2$ denote the first and second invariants of the isochoric deformation tensors, respectively. For simplicity, the

Equation (2) can be written in the polynomial form as suggested by Rivlin[39]:

$$
\begin{aligned}
W &= W_{\mathrm{D}}(\bar{I}_1, \bar{I}_2) + W_I(J) \\
&= \sum_{k+l=1}^{N} C_{kl}(\bar{I}_1 - 3)^k (\bar{I}_2 - 3)^l + \sum_{k=1}^{N} \frac{1}{D_k}(J - 1)^{2k},
\end{aligned}
\tag{3}
$$

where C_{kl} and D_k are material constants, to be determined through fitting, and J is the volume ratio.

Polymeric soft materials are typically treated as incompressible in constitutive models, signifying that their bulk modulus significantly exceeds the shear modulus.[12] This allows the neglect of the volumetric term in the strain energy equation. For this study, the Yeoh model was selected due to its widespread use in accurately predicting the behavior of hyperelastic materials. Specifically, the three-term Yeoh model was employed for this[40,41]:

$$
\begin{aligned}
W &= \sum_{k+l=1}^{N} C_{kl}(\bar{I}_1 - 3)^k (\bar{I}_2 - 3)^l \\
&= C_{10}(\bar{I}_1 - 3) + C_{20}(\bar{I}_1 - 3)^2 + C_{30}(\bar{I}_1 - 3)^3.
\end{aligned}
\tag{4}
$$

In uniaxial tension mode, the relationship between the first strain invariant $\bar{I}_1$ and tensile strain λ is as follows:

$$\bar{I}_1 = \lambda^2 + 2\lambda^{-1}. \tag{5}$$

By taking the partial derivative of the strain energy function with respect to the tensile strain λ, the relationship between tensile stress and tensile strain can be derived, as expressed in Equation (6):

$$\sigma = \frac{\partial W}{\partial \bar{I}_1}\frac{\partial \bar{I}_1}{\partial \lambda} = 2(\lambda - \lambda^{-2})\left[C_{10} + 2C_{20}(\bar{I}_1 - 3) + 3C_{30}(\bar{I}_1 - 3)^2\right]. \tag{6}$$

In uniaxial tension mode, the relationship between the first strain invariant $\bar{I}_1$ and shear strain γ is as follows:

$$\bar{I}_1 = \gamma^2 + 3. \tag{7}$$

By taking the partial derivative of the strain energy function with respect to shear strain γ, we can establish the relationship between shear stress and shear strain.

$$\tau = \frac{\partial W}{\partial \bar{I}_1}\frac{\partial \bar{I}_1}{\partial \gamma} = 2(C_{10}\gamma + 2C_{20}\gamma^3 + 3C_{30}\gamma^5). \tag{8}$$

The stress–strain relationship of a material can be measured in both tensile and shear tests:

$$\sigma = f(\sigma), \tau = f(\gamma). \tag{9}$$

And the experimental data can be utilized to determine the unknown variable C_{i0} in either Equations (6) or (8).

2.2.2 | Viscoelastic part

Unlike crosslinked chains, the unbound chains within the adhesive (free chains), comprised of numerous monomers, experience relaxation and disentanglement phenomena, which play a role in the adhesive's overall viscoelastic properties.[20] The reptation of free chains within the cross-linked network is irreversible and causes energy dissipation (the mechanical response exhibits hysteresis upon cyclic loading), leading to a viscous mechanical behavior.

The viscoelastic phenomena in materials can be described by a generalized Maxwell model[42,43] incorporating velocity-dependent dashpots and displacement-dependent springs, as depicted in

Figure 2b. Mathematically, this can be represented in the form of a Prony series:

$$g(t) = \sum_{i=1}^{N} g_i\left(1 - e^{-\frac{t}{\tau_i}}\right), \tag{10}$$

where, $g(t)$ represents the normalized modulus, t is the time, N is the number of terms in the Prony series, and g_i and τ_i are the parameters to be fitted in the model.

The time-strain or time-stress curves obtained from creep or stress relaxation test can be normalized to obtain the time-modulus relationship:

$$g = g(t). \tag{11}$$

Similarly, the experimental data can be used to fit the unknown variable g_i and τ_i in Equation (10).

We utilized constitutive equations for the material's mechanical response, incorporating hyperelasticity and viscoelasticity. These equations, crucial for finite element simulations, combine the Yeoh model with the Prony series to effectively represent the stress–strain relationship under large strains, deformations, and time effects.

2.2.3 | Parameter calibration

The calibration of constitutive parameters enables the conversion of experimental results into a universal form, recognizable by finite element method (FEM). The primary challenge encountered revolves around maintaining stability when dealing with significant strain levels, where the maximum strain exceeds 500% in the simulation. We utilize shear experimental data obtained at different temperatures to calibrate the hyperelastic model and employ creep data to calibrate the viscoelastic model. This approach enables the derivation of a comprehensive mathematical expression that captures the time-dependent stress–strain relationship of materials subjected to large strains. In contrast to the commonly employed master curve approach in the field of polymers, our approach involves individually fitting the constitutive model at each temperature point. This strategy aims to achieve a more precise and stable model that can provide a more accurate description of the mechanical response under large strains.

2.3 | Verification of constitutive models

The three-point bending test was performed using the Mark-10 ESM303 machine (as depicted in Figure 1),

concurrently with the creation of its FEM model. The sample for the three-point bending consisted of a three-layered laminated plate, with the OCA serving as the middle layer (100 μm), and thin polyethylene terephthalate (PET, 80 μm) comprising the upper and bottom layers.

The geometric model and the elements for this study are illustrated in Figure 1. The direction of the connecting line between the two supports corresponds to the X-direction, while the thickness of the OCA is aligned with the Z-direction, and the width extends along the Y-direction. The indenter and supports in this investigation possessed diameters of 5 and 10 mm, respectively, with a span of 20 mm, as depicted in Figure 6a. The dimensions of the bending sample were 9.6 mm in width and 50 mm in length. To enhance computational efficiency, symmetry was applied in both the X and Y directions, resulting in a model material measuring 4.8 mm in width and 25 mm in length. The indenter and supports were treated as rigid bodies. The modulus of polyethylene glycol terephthalate (PET), determined through tensile testing, was found to be 2700 MPa with a Poisson's ratio of 0.3887, and a linear elastic model was employed for PET. In the case of the OCA adhesive's constitutive model, fitted parameters were utilized.

As shown in Figure 1, the model is discretized into mesh layers with a thickness of 20 μm in the direction of the thickness. In the X and Y directions, the mesh is divided according to the thickness of 5:1 with a total of 15,600 elements. The element type was chosen C3D8R: three-dimensional, eight-node, reduced integration element. The boundary conditions are symmetric in the X and Y directions, and the supports were fixed. The indenter descends by 5 mm at a speed of 10 mm/min and subsequently ascends at the same speed (loading–unloading). Alternatively, the indenter can descend and be held for a specified period (e.g., 10, 60, 300, 600, and 1800s) before returning (loading–holding–unloading). The convergence is satisfactory, and the computation time approximately amounts to 2 h.

3 | RESULTS AND DISCUSSION

3.1 | Experimental results

3.1.1 | Strain rate

Figure 3 primarily illustrates the stress–strain relationship under varying strain rates (0.01, 0.1, 1, and 5 s^{-1}). in both tensile and shear testing, the material exhibits rate dependence at different strain rates and temperatures,

with a higher strain rate corresponding to a greater modulus. Significantly, at the same strain level, the stress value in the experiment with the highest strain rate of 5 s^{-1} is approximately twice that of the experiment with the lowest strain rate of 0.01 s^{-1}. This pattern persists across various temperatures and loading conditions. Among these results, the shear experiment conducted at a high strain rate of 5 s^{-1} is particularly noteworthy, as it aligns with the actual working conditions of folding mobile phones. In such devices, users complete the folding process within two seconds, resulting in a maximum strain approaching 1000%.

Figure 3a illustrates the tensile test results under various strain rates at a temperature of 25°C. Figure 3b–d illustrates the nominal stress–strain curves from shear tests conducted under various strain rates at temperatures of 25, 65, and 80°C, respectively. Figure 3b–d is presented in a uniformly scaled horizontal and vertical coordinate system for the purpose of direct comparison. While the overall trend of change remains consistent, subtle distinctions are discernible. Particularly at high temperatures (see Figure 3b,d), the stress–strain curves for the material at various strain rates exhibit a closer alignment. This suggests a diminishing influence of viscoelastic properties with rising temperatures. Given the impracticality of OCA material usage at high temperatures, it is plausible to disregard viscoelasticity in FEM conducted under extreme environmental conditions such as high temperatures.

3.1.2 | Temperature sensitive

Figure 4 primarily illustrates the results of simple shear, tensile, and creep tests under varying temperatures. Materials display notable distinctions at various temperatures and manifest considerable temperature sensitivity.

Figure 4a presents the shear data obtained at −40, −20, 0, 25, 65, and 80°C, with a strain rate of 5 s^{-1}. It can be observed that the shear modulus of OCA increases as the temperature decreases. Notably, at the lowest temperature of −40°C, the shear modulus was approximately 10 times higher than the highest temperature (80°C). In this experiment, there is little difference in shear modulus between 65 and 80°C. The shear modulus decreases from 39.4 kPa at 0°C to 34.9 kPa at 25°C and 20.0 kPa at 65°C. However, at −20 and −40°C, the shear modulus (60.8 kPa, 262.3 kPa, respectively) exhibits significant changes. Therefore, the material remains relatively stable above 0°C. Additionally, when comparing these results with Figure 3b–d (shear experiments at different rates), the shear modulus of the material increases as the temperature decreases.
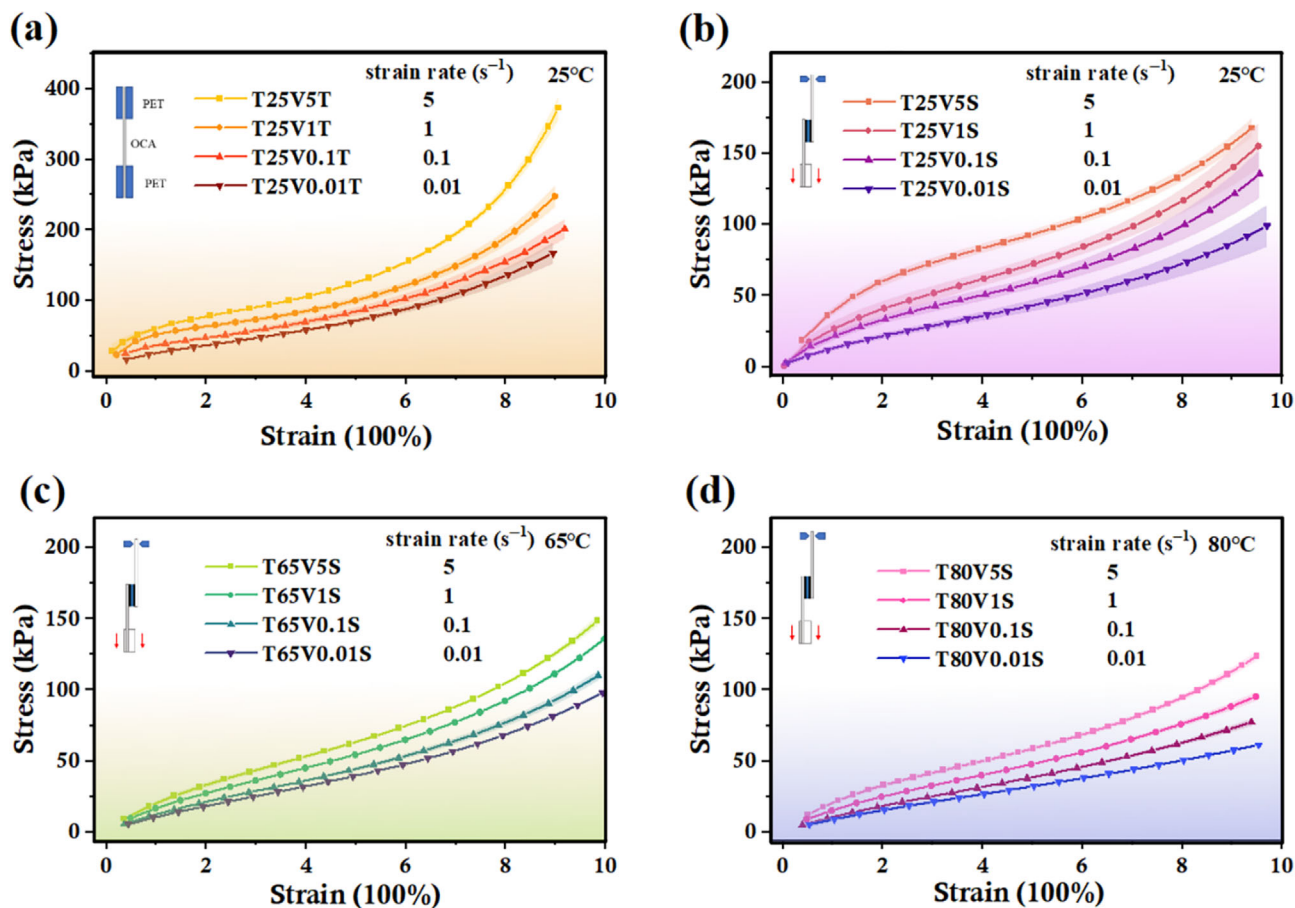
FIGURE 3 (a) Tensile test at different strain rates (0.01, 0.1, 1, and 5 s^{-1}) in 25°C, shear test at different strain rates (0.01, 0.1, 1, and 5 s^{-1}) and temperatures (b) 25, (c) 65, and (d) 80°C. [Color figure can be viewed at wileyonlinelibrary.com]

Figure 4b showcases the low-temperature tensile test conducted using DMA with a strain rate of 0.1 s^{-1}. Due to limitations in the measuring range and working space, the maximum strain achieved was 350%. Similar to the shear test in Figure 4a, the modulus (0.1 s^{-1} and 20% strain) of the material significantly improves at −40°C (249.3 kPa).

The results of creep testing were presented in Figure 4c, where the time-strain curve was plotted over a duration of 10 h. The OCA demonstrated distinct behavior at different temperatures: 25, 65, and 80°C. At 25 and 65°C, the OCA exhibits two distinct stages: primary and secondary. In the primary stage, the OCA undergoes rapid exponential strain growth. This initial stage is followed by secondary step, characterized by a constant strain rate and a slower linear increase in strain until it reaches a steady state. The OCA demonstrates a stable response under these conditions. However, at 80°C, the behavior of the OCA is notably different. It experiences rapid strain growth, leading to failure at 10,000 s (2.7 h). This suggests that the OCA is sensitive to temperature, particularly under high-stress creep loading conditions. Even with a relatively small temperature increase of only

15°C, the material experiences accelerated failure. This indicates that the OCA is not suitable for long-term use under high-stress, and high-temperature conditions. Generally, the creep testing results reveal that the OCA undergoes distinct stages of strain growth at different temperatures. The material performs well at lower temperatures but exhibits rapid failure at elevated temperatures, highlighting its limitations in high-stress, high-temperature applications.

3.1.3 | Humidity

Figure 5 shows the configuration method of humidity environment and the experimental results under high humidity. To meet the requirements of the electronics industry for a working environment with 95% RH and temperatures of 65 to 80°C, a self-made high-temperature and high-humidity environmental chamber was utilized which is shown in Figure 5a,b. The humidity experiment consisted of two parts: one focused on room temperature and high humidity (25°C, 95% RH), and the other on high temperature and high humidity (80°C, 95% RH).
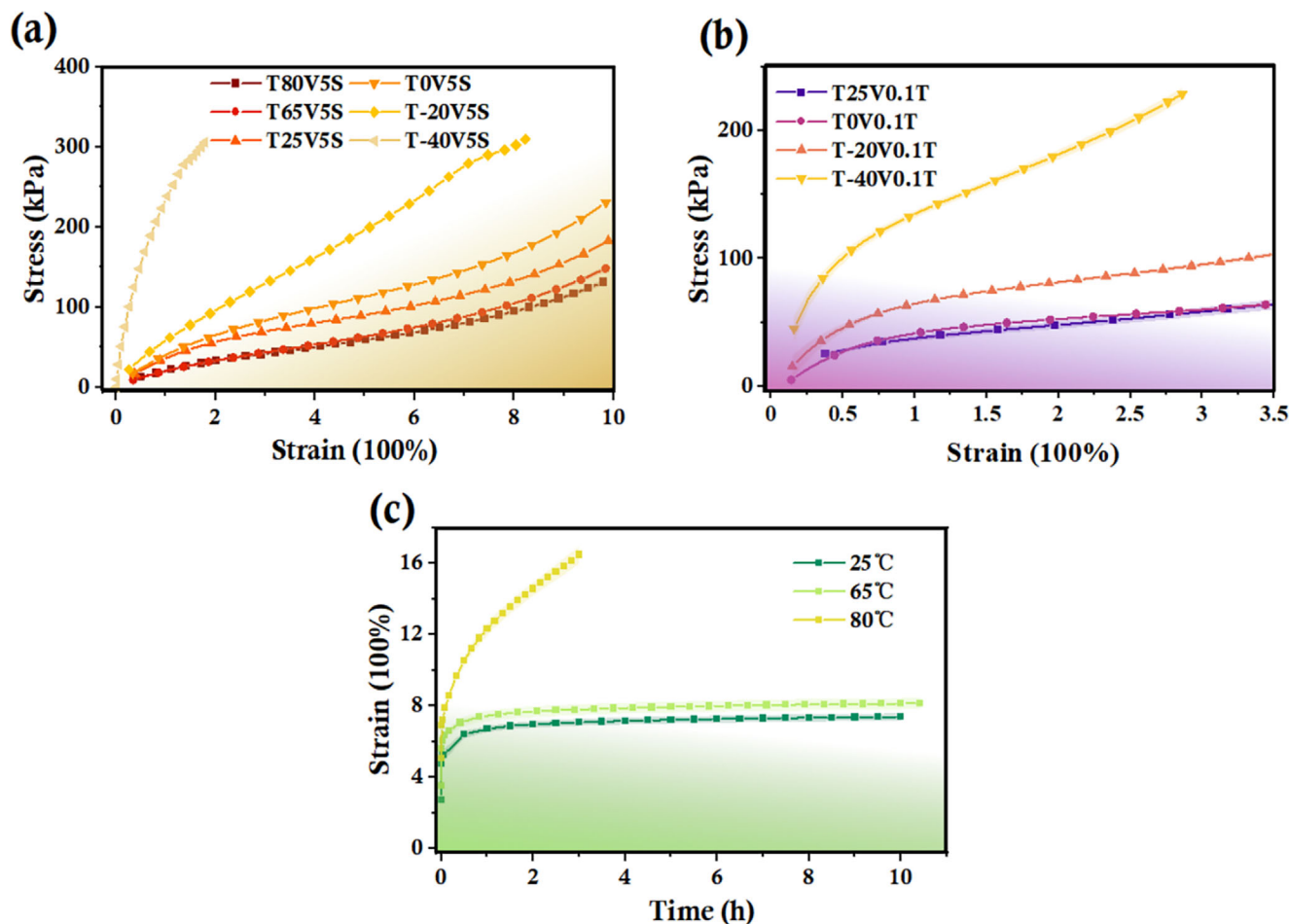
FIGURE 4 (a) Simple shear results at different temperatures (-40, -20, 0, 25, 65, and 80°C), (b) Low temperature tensile results (-40, -20, 0, and 25°C), and (c) creep test under 50 kPa stress at different temperatures (25, 65, and 80°C). OCA, optically clear adhesive. [Color figure can be viewed at wileyonlinelibrary.com]

In the room temperature and high humidity condition, an industrial humidifier was used to blow moisture onto the samples, as shown in Figure 5a. On the other hand, the high temperature and high humidity condition involved the use of a steam engine and a custom-made environmental box, as shown in Figure 5b. Figure 5c–e displays the tensile experiments conducted at different strain rates under high temperature and high humidity conditions (80°C, 95% RH). The strain rates used were 1, 2, and 5 s^{-1}. Similar to the high temperature and humidity environment, the OCA's modulus did not undergo significant changes, and the nominal stress–strain curve remained roughly the same. However, the material's ultimate fracture strength was affected, with fractures occurring primarily at a strain of 1500%. The OCA experienced degradation when exposed to water vapor erosion in a high temperature and humidity environment. During the service life of the OCA, it is encapsulated within the OLED screen and is not typically exposed to moisture in the environment. However, in the experiment, moisture was directly blown onto the OCA

adhesive, making the experimental conditions more severe than the actual environment.

In order to study the response of OCA to humidity at room temperature, we conducted tensile tests under both room humidity (approximately 40% RH) and high humidity conditions (95% RH), as shown in Figure 5f. The results indicated that humidity had a minimal effect on the mechanical properties of OCA, with the nominal stress–strain curve remaining similar to that observed in the room humidity experiment. However, when comparing the previous test results at high temperatures, we find that OCA exhibits minimal sensitivity to humidity at room temperature. Its sensitivity to humidity becomes more pronounced at high temperatures.

3.1.4 | Poisson's ratio

Figure 7g depicts the Poisson's ratio of OCA samples under uniaxial tension tests. During the tension test, the OCA was subjected to a macro-strain of 500%. The initial
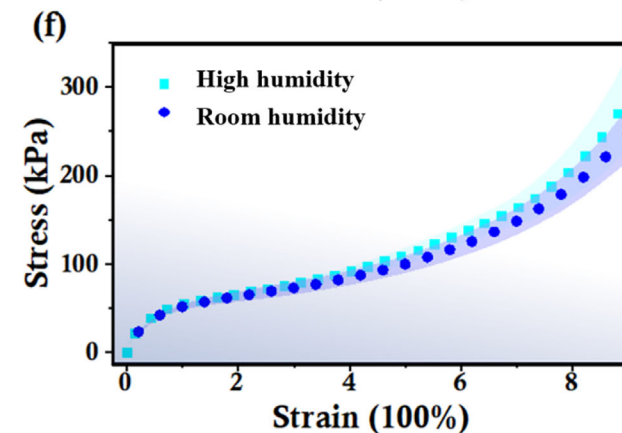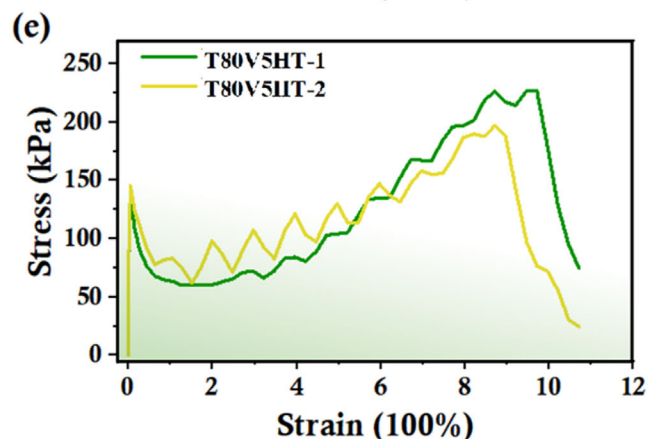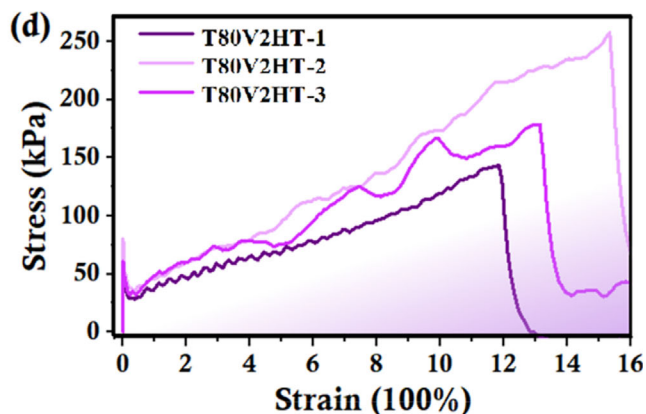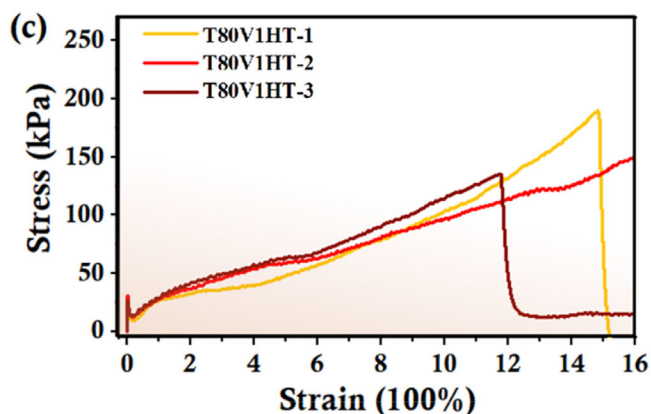
FIGURE 5 Experimental setting of tensile test (a) Room temperature and high humidity (25°C, 95% RH), (b) high temperature and high humidity (80°C, 95% RH), tensile results at (c–e) different strain rates under high temperature and high humidity (80°C, 95% RH), (f) tensile results at room temperature under both room humidity (about 40% RH) and high humidity conditions (95% RH). [Color figure can be viewed at wileyonlinelibrary.com]

Poisson's ratio is observed to approximate 0.5, gradually decreasing to 0.46 with increasing strain while maintaining stability. It is noteworthy that the calculation of Poisson's ratio in Equation (1) is based on the assumption of small strains, yielding greater accuracy (~0.5) at lower strain levels. However, as strain increases, errors become increasingly evident. Nevertheless, the Poisson's ratio of

OCA is markedly higher than that of steel (~0.3), approaching 0.5, positioning it as an almost incompressible.

Additionally, Figure 7g presents local axial strain cloud maps at various macroscopic strain-loading levels (ε of 1, 2, 3, 4, and 5). The distribution of uniaxial tensile strain indicating that the strain distribution within the
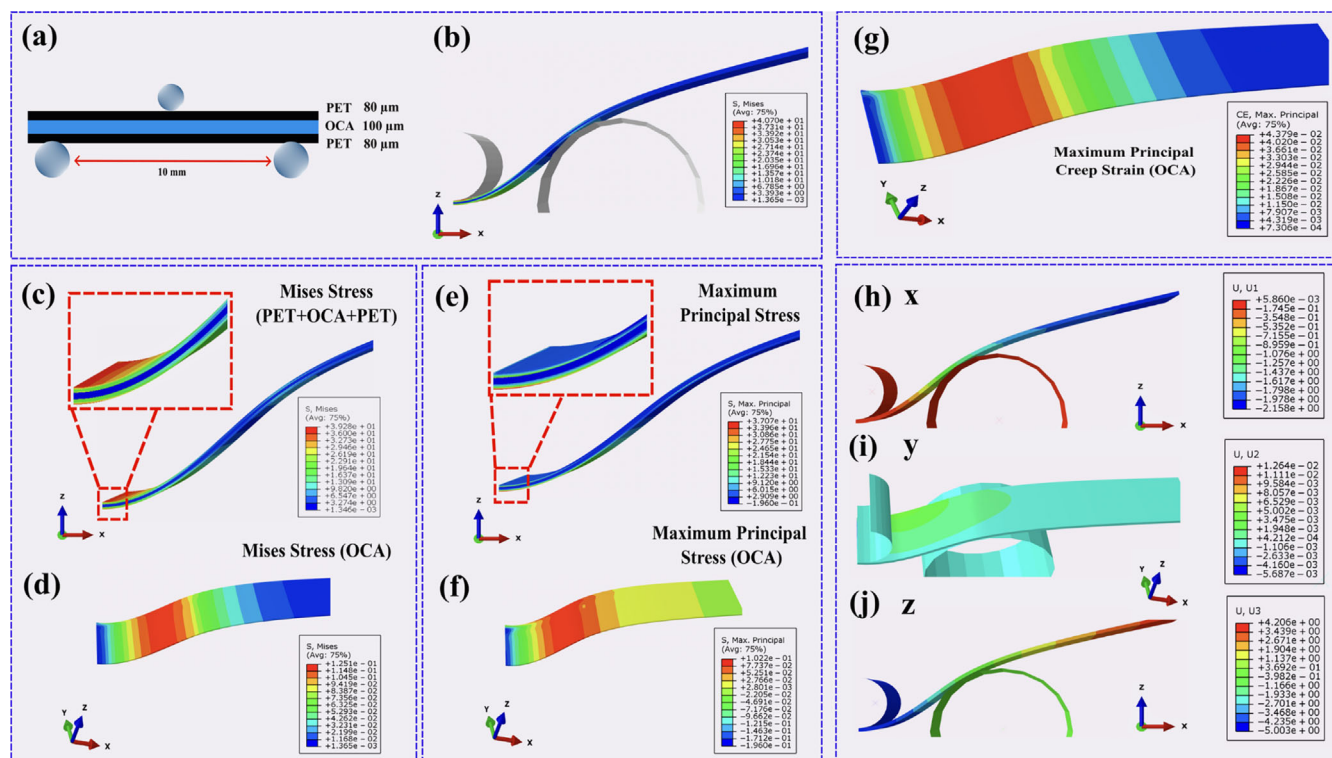
FIGURE 6 (a) Schematic diagram of three-point bending test, (b) three-point bending specimen after deformation, Mises stress of (c) PET + OCA + PET composite laminated structure, (d) OCA layer, maximum principal stress of (e) composite laminated structure PET + OCA + PET, (f) OCA layer, (g) creep strain (OCA), deformation in three direction (h) X, (i) Y, and (j) Z direction displacement. [Color figure can be viewed at wileyonlinelibrary.com]

OCA is completely uniform. The uniform distribution of local axial strain in the OCA suggests that strain is evenly spread, and the dimensional design of the test samples allows for an accurate representation of the material's macroscopic mechanical properties.

3.2 | Calibration parameters

The fitted hyperelastic and viscoelastic parameters are presented in Tables 2 and 3, respectively. It is worth noting that the unit of C_{i0} is Pascal, g_i is dimensionless, and the unit of τ_i is seconds. All hyperelastic constitutive models have undergone stability checks, and the fitted R-squared values are above 0.98. These fitted parameters can be subsequently employed in finite element simulations of flexible devices. This utilization offers useful guidance to researchers regarding the mechanical response of OCA materials under various temperature conditions, including low, room, and high temperatures. In general, a full or reduced polynomial material model is considered stable when all the coefficients (C_{ij}) are positive. However, the presence of some negative coefficients does not necessarily imply model instability. In the case of the Yeoh model, the negative C_{20} coefficient is

commonly employed to capture the *S*-shaped feature of the stress–strain curve (Table 2).

3.3 | Simulation and verification

Figure 6 illustrates the results of stress and strain distribution obtained through FEM. In particular, Figure 6b presents the overall displacement curve of the model in response to a 5 mm load applied as an input displacement. The model rotates around the lower support, aligning with the experimental observations (duration 30 s). Figure 6c illustrates the Von Mises stress for both OCA and PET materials. It is evident that the stress levels in OCA are comparatively low, whereas PET exhibits significantly higher stress levels (higher order of magnitude). Figure 6d depicts the Von Mises stress distribution for the OCA sample when subjected to a 5 mm load, with the maximum stress value occurring at the contact point with the lower support. To further analyze the stress distribution, the maximum principal stress diagrams for both OCA and PET have been shown in Figure 6e. Additionally, Figure 6f zooms on the maximum principal stress of the OCA material. Figure 6g illustrates the maximum principal creep strain distribution of the OCA
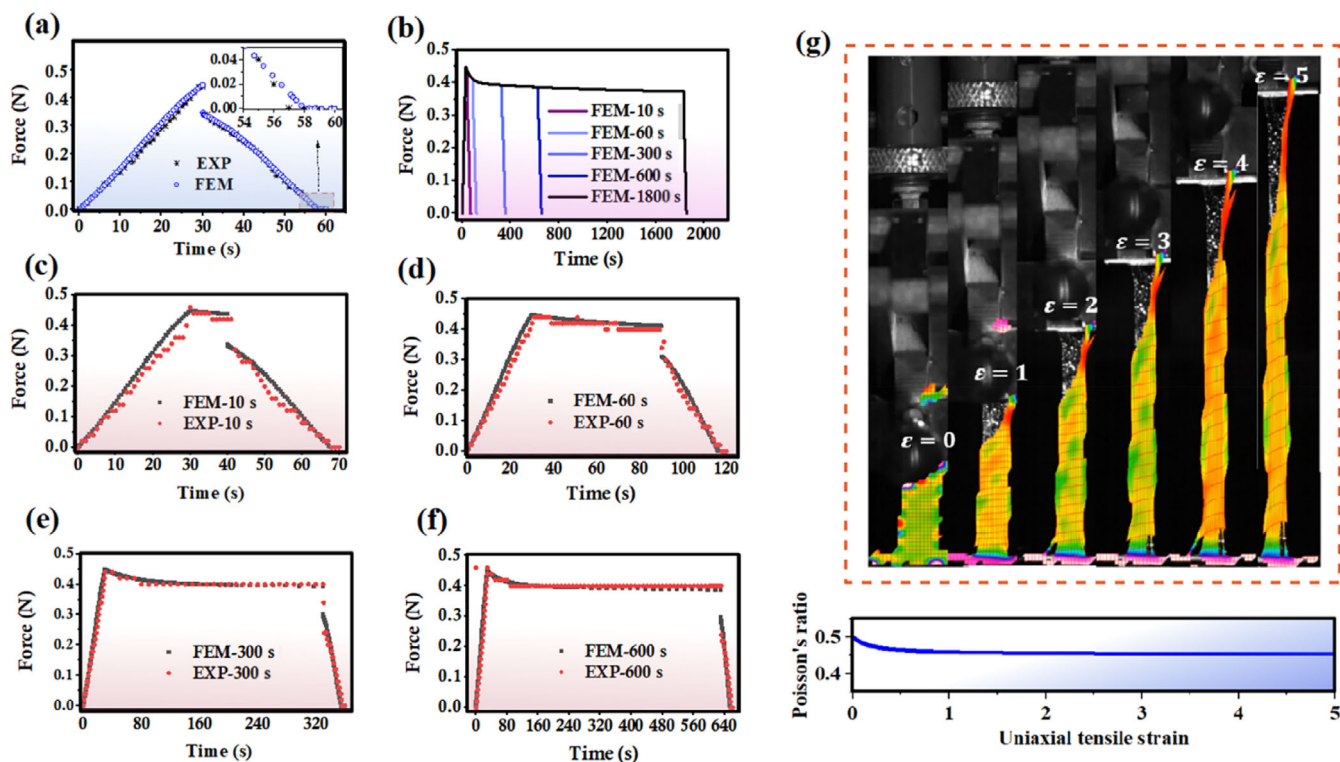
FIGURE 7 Comparison of (a) three-point bending test (loading–unloading), (b) loading–holding–unloading experimental results and FEM, loading–holding–unloading experimental results and FEM in various holding time of (c) 10, (d) 60, (e) 300, and (f) 600 s. (g) DIC speckle distribution and Poisson's ratio. OCA, optically clear adhesive. [Color figure can be viewed at wileyonlinelibrary.com]

TABLE 2 Calibration of Hyperelastic material parameters using shear tests.

	C_{10}/Pa	C_{20}/Pa	C_{30}/Pa
−40°C	42,523	−1192	42.2
−20°C	19,645	−488	10.9
0°C	12,539	−303	6.4
25°C	42,183	−386	1.9
65°C	41,635	−282	1.3
80°C	22,558	−191	0.9

material, which closely follows the Mises stress distribution observed in Figure 6d. Finally, Figure 6h–j provides an overview of the overall displacement in the X, Y, and Z directions, respectively under same condition. These displacement curves offer a comprehensive understanding of the model's response to the loading conditions.

The experimental and FEM results of time-force curve (loading–unloading) were shown in Figure 7a. In both the experimental tests and numerical simulations, a sudden change in the applied load force was observed during the loading and unloading transition, primarily due to the viscoelastic nature of the OCA. During the loading process, the strain rate was positive, and the material's

viscous and elastic forces acted in the same direction to counterbalance the external load. However, at the loading and unloading transition, the strain rate shifts from positive to negative, leading to a reversal in the direction of the elastic force. At this juncture, the viscous force and the external load work in concert to balance the elastic force, resulting in a sudden decrease in the external load. During the unloading stage, the direction of the viscous force opposes that of the elastic force. When the elastic force becomes insufficient to counteract the viscous force, the force between the indenter and the material diminishes to zero, and the indenter separates from the material (as observed at 60 s in the experiment). This phenomenon indicates that energy loss takes place as a result of frictional dissipation in the molecular chain during both loading and unloading, and this energy loss does not recover along the unloading path. The successful prediction of these phenomena demonstrates the effectiveness of the calibration of constitutive mode. This model accurately captured the complex behavior of the OCA material, including the effects of viscoelasticity, elastic forces, and energy dissipation during loading and unloading.

Additionally, the study examined the stress relaxation behavior of the OCA material under a loading-

TABLE 3 Viscoelastic parameter calibration using creep tests.

		1	2	3	4	5
25°C	g_i	0.634611	0.073990	0.072129	0.059054	0.109971
	τ_i/s	0.0001	0.006366	0.100356	1.898110	3273
65°C	g_i	0.778926	0.018575	0.036045	0.031520	0.084875
	τ_i/s	0.0001	0.018972	0.100132	3.908512	4253
80°C	g_i	0.560955	0.058106	0.065121	0.078537	0.085155
	τ_i/s	0.0007	0.067703	0.300000	7.000000	74,033

holding-unloading condition (Figure 7b). This involves loading the material, maintaining the displacement for a specific duration (10, 60, 300, 600, and 1800 s), and then unloading that. The simulation results (Figure 7b), indicating that the material undergoes stress relaxation after the corresponding holding time. Prior to that point, the force-displacement behavior for each working condition remained consistent. Comparing the simulation results with the experimental data, a relatively close agreement was observed, achieving an accuracy of approximately 90% (as shown in Figure 7c–f).

4 | CONCLUSION

In this study, the large strain mechanical behavior of OCA for flexible electronic devices under various temperature, strain rate, and humidity conditions was meticulously investigated through experimental and numerical methods. A universal method for analyzing the mechanical properties of soft materials like OCA was presented, encompassing material testing, calibration of constitutive parameters, verification, and their integration into finite element simulation. The main conclusions can be summarized as follows:

1. The material exhibits significant temperature sensitivity and viscoelasticity in its mechanical response under various loading conditions. Within the extreme temperature range relevant to foldable flexible devices (−40 to 80°C), the modulus of OCA undergoes an approximate 10-fold reduction. Additionally, when simulating the strain rate during the rapid folding of the device ($5\,\mathrm{s}^{-1}$), the modulus of OCA is roughly twice that observed under quasi-static loading conditions ($0.01\,\mathrm{s}^{-1}$). Simultaneously, we observed that humidity has a negligible effect on the modulus of the material. However, it is noteworthy that water vapor can corrode the material, thereby influencing its strength.

2. The OCA can be considered almost incompressible based on DIC tests, with a Poisson's ratio stabilizing around 0.46 at large strains. This suggests that the volume term in the hyperelastic constitutive equation can be ignored.

3. The hyperelastic and viscoelastic constitutive models were fitted at various temperatures, providing a valuable reference for future researchers studying the response of flexible devices under extreme environments. The selected constitutive model faithfully replicates the experimental observations, demonstrating a remarkable alignment in both numerical values and trends. The macroscopic mechanical behavior observed in three-point bending tests further validates the model's accuracy, achieving an approximate 90% match with experimental data.

However, the model and simulation presented in this paper still have some limitations in predicting OCA behavior at large strains. In this constitutive model, we focus on stress–strain relationships, excluding damage models. However, large strain processes disrupt the molecular network of polymer materials. During loading, necking may occur, leading to localized deformation and making the nominal stress–strain curve insufficient to capture the material's true state, thus necessitating the calculation of the true stress–strain curve. While phenomenological constitutive models based on polynomials are simple and broadly applicable, they fail to capture the material's microscopic physical response. Therefore, a physical constitutive model tailored to the molecular network and microstructure of the material is needed for accurate predictions under large deformation. In the future, more efforts should be directed toward understanding the microscopic mechanical mechanisms of OCA and establishing a connection with its macroscopic response. Additionally, the phenomenon of water vapor erosion in polymer networks needs to be explained from a microscopic perspective as well to elucidate its impact on strength reduction.

AUTHOR CONTRIBUTIONS
Jinrui Cao: Conceptualization (equal); formal analysis (equal); investigation (equal); methodology (equal);

DATA AVAILABILITY STATEMENT

The data that support the findings of this study are available from the corresponding author upon reasonable request.

ORCID

Jinrui Cao https://orcid.org/0000-0001-6013-1115
Jiayi Hu https://orcid.org/0000-0003-4263-9454
Hongyan Yuan https://orcid.org/0000-0001-8225-0211

REFERENCES

[1] J. Back, Y. Kwon, H. Cho, H. Lee, D. Ahn, H. Kim, Y. Yu, Y. Kim, W. Lee, M. S. Kwon, _Adv. Mater._ **2023**, _35_, 2204776.

[2] D. Lim, M.-J. Baek, H.-S. Kim, C. Baig, D. W. Lee, _Chem. Eng. J._ **2022**, _437_, 135390.

[3] J. T. Abrahamson, H. Z. Beagi, F. Salmon, C. J. Campbell, in _Luminescence - OLED Technology and Applications_ (Ed: S. Pyshkin), IntechOpen, Rijeka **2020**.

[4] S.-E. Ouassil, A. El Magri, H. R. Vanaei, S. Vaudreuil, _J. Appl. Polym. Sci._ **2023**, _140_, e53353.

[5] C.-F. J. Kuo, J.-B. Chen, S.-H. Chang, _J. Appl. Polym. Sci._ **2018**, _135_, 46277.

[6] A. R. Cho, E. H. Kim, S. Y. Park, L. S. Park, _Synth. Met._ **2014**, _193_, 77.

[7] W. Jo, K. Jeong, Y.-S. Park, J.-I. Lee, S. Gap Im, T.-S. Kim, _Chem. Eng. J._ **2023**, _452_, 139050.

[8] M. Nishimura, K. Takebayashi, M. Hishinuma, H. Yamaguchi, A. Murayama, _J. Soc. Inf. Disp._ **2019**, _27_, 480.

[9] Y.-F. Niu, S.-F. Liu, J.-Y. Chiou, C.-Y. Huang, Y.-W. Chiu, M.-H. Lai, Y.-W. Liu, _J. Soc. Inf. Disp._ **2016**, _24_, 293.

[10] Y. Shi, J. A. Rogers, C. Gao, Y. Huang, _J. Appl. Mech._ **2014**, _81_, 114501.

[11] T.-I. Lee, W. Jo, W. Kim, J.-H. Kim, K.-W. Paik, T.-S. Kim, _ACS Appl. Mater. Interfaces_ **2019**, _11_, 13416.

[12] C. Creton, M. Ciccotti, _Rep. Prog. Phys._ **2016**, _79_, 046601.

[13] M. M. Azrain, M. R. Mansor, G. Omar, S. H. S. M. Fadzullah, S. R. Esa, L. M. Lim, D. Sivakumar, M. N. A. Nordin, _Synth. Met._ **2019**, _247_, 191.

[14] Y. Zhang, S. Wang, F. Dong, Y. Sun, C. Sheng, K. Ma, Z. Tian, Z. Qian, C. Wong, S. Liu, _Micromachines_ **2022**, _13_, 301.

[15] J. Zhang, H. Jiang, C. Jiang, G. Kang, F. Lu, _Polym. Test._ **2015**, _44_, 8.

[16] S. H. Han, J. H. Shin, S. S. Choi, _Sci. Rep._ **2023**, _13_, 5697.

[17] Q. Wang, W. Su, W. Zhang, Z. Zhang, B. Wang, D. Zhang, F. Zhang, _J. Eng._ **2022**, _2022_, 1.

[18] B. Yu, J. Chen, D. Chen, R. Chen, Y. Wang, X. Tang, H.-L. Wang, L.-P. Wang, W. Deng, _Phys. Fluids_ **2021**, _33_, 092106.

[19] S. Chen, D. Fan, C. Gui, _Polym. Test._ **2023**, _120_, 107971.

[20] T. Zhao, J. Cao, X. Li, M. Xia, B. Xue, H. Yuan, _Extreme Mech. Lett._ **2022**, _51_, 101594.

[21] Y. Xiang, D. Zhong, P. Wang, T. Yin, H. Zhou, H. Yu, C. Baliga, W. Yang, _J. Mech. Phys. Solids_ **2019**, _128_, 208.

[22] H. Chen, L. R. Hart, W. Hayes, C. R. Siviour, _Polymer_ **2021**, _221_, 123607.

[23] M. Fujita, A. Takemura, H. Ono, M. Kajiyama, S. Hayashi, H. Mizumachi, _J. Appl. Polym. Sci._ **2000**, _75_, 1535.

[24] X. Li, W. Li, M. Huo, J. Xu, _J. Appl. Polym. Sci._ **2023**, _140_, e53376.

[25] W. Wang, Y. Jia, H. Li, M. Jiang, Z. Zhang, _J. Soc. Inf. Disp._ **2021**, _29_, 723.

[26] Y. Jia, Z. Liu, D. Wu, J. Chen, H. Meng, _Org. Electron._ **2019**, _65_, 185.

[27] L. Guo, J. Liu, H. Xia, X. Li, X. Zhang, H. Yang, Y. Yang, _Polym. Test._ **2022**, _109_, 107528.

[28] H. Chen, P. Song, T. Commins, A. Graham, A. R. Trivedi, C. R. Siviour, _Polymer_ **2022**, _249_, 124860.

[29] J. Edwin Raja Dhas, K. Anton Savio Lewise, N. K. Kulandaiyappan, V. Raja, C. A. Saleel, M. Alwetaishi, B. S. Arputharaj, A. M. H. Deif, H. A. Z. AL-bonsrulah, _J. Mater. Res. Technol_ **2023**, _26_, 6084.

[30] G. Marckmann, E. Verron, _Rubber Chem. Technol._ **2006**, _79_, 835.

[31] K. Hyun, M. Wilhelm, C. O. Klein, K. S. Cho, J. G. Nam, K. H. Ahn, S. J. Lee, R. H. Ewoldt, G. H. McKinley, _Prog. Polym. Sci._ **2011**, _36_, 1697.

[32] N. L. M. Hafiz, P. M. Tahir, L. S. Hua, Z. Z. Abidin, F. A. Sabaruddin, N. M. Yunus, U. H. Abdullah, H. P. S. Abdul Khalil, _J. Mater. Res. Technol._ **2020**, _9_, 6994.

[33] S. Sadeghzade, J. Cao, D. Zhang, P. Dong, J. Hu, A. Es'haghioskui, H. Yuan, _Eur. Polym. J._ **2023**, _197_, 112337.

[34] P. Dong, R. Hou, J. Hu, C. Lin, Y. Liu, L. Qin, _Polym. Test._ **2023**, _122_, 108015.

[35] O. Hasturk, J. K. Sahoo, D. L. Kaplan, _Polymer_ **2023**, _281_, 126129.

[36] B. T. Poh, H. K. Kwo, _J. Appl. Polym. Sci._ **2007**, _105_, 680.

[37] K. Y. Volokh, _Int. J. Solids Struct._ **2007**, _44_, 5043.

[38] J. Cao, A. Es'haghioskui, P. Dong, Z. Gong, H. Yuan, _Displays_ **2024**, _83_, 102722.

[39] R. S. Rivlin, A. G. Thomas, _J. Polym. Sci._ **1953**, _10_, 291.

[40] C. Zhong, X. Peng, C. Li, Y.-Q. Wan, S.-M. Xue, J. Lu, Z.-Q. Liu, R. Sun, N. Liu, B. Gao, H. Chang, _2022 23rd International Conference on Electronic Packaging Technology (ICEPT)_, IEEE, Dalian, China **2022**, p. 1.

[41] C. Zhong, C. Li, L. Lu, Y. Wang, G. Li, P. Zhu, J. Lu, R. Sun, C.-P. Wong, *2021 22nd International Conference on Electronic Packaging Technology (ICEPT)*, IEEE, Xiamen, China **2021**, p. 1.

[42] Y. Xiang, D. Zhong, P. Wang, G. Mao, H. Yu, S. Qu, *J. Mech. Phys. Solids* **2018**, *117*, 110.

[43] Y. Xiang, D. Zhong, S. Rudykh, H. Zhou, S. Qu, W. Yang, *J. Appl. Mech.* **2020**, *87*, 110801.